Academic Journal of Science and Technology
ISSN: 2771-3032 | Vol. 15, No. 2, 2025

Monitoring of Mining-Induced Surface Subsidence Based on Multi-Source Data Fusion

Jiankun Han[1, *]

[1]School of Surveying and Land Information Engineering, Henan Polytechnic University, Jiaozuo, Henan 454003, China
[*]Corresponding author: Jiankun Han; Email: 212204010036@home.hpu.edu.cn

Abstract: A method for extracting mining-induced surface subsidence based on multi-source data fusion is proposed by integrating the advantages of InSAR, PIM, and UAV technologies. This approach first employs InSAR to obtain time-series cumulative subsidence basins and constructs constraint conditions to distinguish between high-gradient deformation zones, enabling the differentiation of subsidence edges and centers. In the subsidence edge areas, InSAR monitoring results are retained, while in the central zones with large-gradient subsidence, a weighted fusion of PIM and UAV data is conducted to establish a subsidence basin model for the mining working face. Subsequently, spatial interpolation is applied to derive continuous surface subsidence information in a geographic coordinate system, ultimately generating a complete surface subsidence map of the mining area. The method is validated using Sentinel-1A satellite imagery, UAV data, and leveling measurements from the 120101 working face of the Yangchangwan Coal Mine in the Ningdong mining area. The results demonstrate that this method effectively compensates for the limitations of using InSAR, PIM, or UAV data individually, enhances monitoring capability in high-gradient subsidence areas, and enables the acquisition of more accurate and spatially continuous surface subsidence information.

Keywords: PIM; DInSAR; UAV; Mining subsidence; Large gradient deformation.

1. Introduction

Surface subsidence in mining areas is a common geological phenomenon during mining activities. Its formation mechanism is complex, involving multiple processes such as rock stratum movement, surface deformation, and the evolution of underground voids[1]. Surface subsidence not only affects the ecological environment of the mining area but may also threaten the safety of infrastructure such as roads, buildings, and pipelines, and even trigger geological disasters, posing significant risks to production and daily life[2–3]. Therefore, monitoring surface subsidence in mining areas is of great importance for ensuring safe mining operations, optimizing mine design, assessing environmental impacts, and supporting disaster prevention and mitigation[4–6].

At present, surface subsidence monitoring in mining areas mainly relies on conventional ground-based measurement techniques and remote sensing technologies. Traditional methods such as leveling, total station surveys, and Global Navigation Satellite System (GNSS) measurements[7–10] can provide highly accurate surface subsidence data. However, these techniques are constrained by their point-based nature, resulting in low spatial resolution and limited capability to capture continuous deformation over large areas. Moreover, these methods require manual measurements, which are time-consuming and labor-intensive. In complex terrains such as mining and collapse zones, field measurements are often difficult to conduct and pose safety risks.Remote sensing technologies, especially Interferometric Synthetic Aperture Radar (InSAR), have been increasingly applied in mining subsidence monitoring in recent years[11–14]. InSAR offers all-weather, wide-area, and high-precision monitoring capabilities and enables time-series monitoring over extended periods. However, in areas with large-gradient subsidence, the rapid surface deformation may cause coherence loss and phase unwrapping errors, thereby reducing monitoring accuracy[15–17]. In addition, traditional InSAR methods primarily capture one-dimensional deformation along the line-of-sight (LOS) direction, which cannot directly provide three-dimensional subsidence information. Deriving vertical deformation typically requires multi-track data and complex inversion procedures[18–20].

To address the limitations of single methods, the Probability Integral Method (PIM) has been widely used for subsidence prediction in mining areas. PIM is an empirical model-based approach that estimates subsidence basins based on mining parameters and the mechanical properties of rock strata, calculating key indicators such as subsidence center, extent, and gradient[21–22]. Since PIM is based on mathematical modeling, it can deliver high temporal resolution predictions and is unaffected by coherence and other remote sensing conditions. However, PIM still faces certain limitations in practical applications: its model relies on empirical parameters and may not adapt well to complex geological conditions, making it difficult to accurately reflect real subsidence processes[23–25]. Moreover, PIM does not inherently incorporate deformation measurements from remote sensing, limiting its overall accuracy.With the development of UAV-based surveying technologies, UAV photogrammetry and LiDAR have been increasingly applied to surface deformation monitoring[26–31]. UAV measurements can rapidly obtain high-resolution, high-accuracy topographic data, providing an effective supplement for monitoring subsidence in complex terrain. Particularly in areas with large-gradient subsidence, UAV data can compensate for data loss in InSAR due to coherence degradation[32–35] and offer high-precision topographic information to optimize PIM models[36–39].

Therefore, how to effectively integrate InSAR, PIM, and UAV measurement data to enhance the accuracy and robustness of mining subsidence monitoring has become a critical research focus.In response to the challenges of monitoring large-gradient subsidence in mining areas, this study proposes a surface subsidence monitoring method that

integrates InSAR, PIM, and UAV data. The method first utilizes InSAR to obtain time-series subsidence information and constructs deformation gradient-based constraints to divide the subsidence region into edge and center zones. In the subsidence edge zones, InSAR results are directly used, while in the central zones with large-gradient subsidence, a PIM-based subsidence basin model is established and optimized using UAV data to improve monitoring accuracy. Subsequently, continuous subsidence information in a geographic coordinate system is obtained through data fusion and spatial interpolation, ultimately generating a complete surface subsidence map for the mining area.

2. Study Area and Data Sources

2.1. Study Area

The Yangchangwan Coal Mine is located in the Ningdong Coalfield of Yinchuan City, Ningxia Hui Autonomous Region, China. The mining area lies on the southwestern edge of the Mu Us Desert and is characterized by aeolian landforms consisting of desert and grassland, belonging to the arid grassland-desert transition zone. Most of the minefield is covered by mobile sand dunes, with sparse surface vegetation and generally flat terrain with gentle undulations. The highest elevation within the mining area reaches 1,502 meters, located in the southern hilly region, while the lowest elevation is 1,395 meters. The general elevation ranges between 1,410 and 1,470 meters.In this study, the 120101 working face of the Yangchangwan Coal Mine was selected as the research target. This working face is approximately 195 meters wide and 2,900 meters long, with a coal seam dip angle of about 8° and an average mining depth of approximately 355 meters. The average daily advancement rate is around 8 meters. Figure 1 shows the geographical extent and basic features of the study area, with the white lines indicating the mining boundaries.

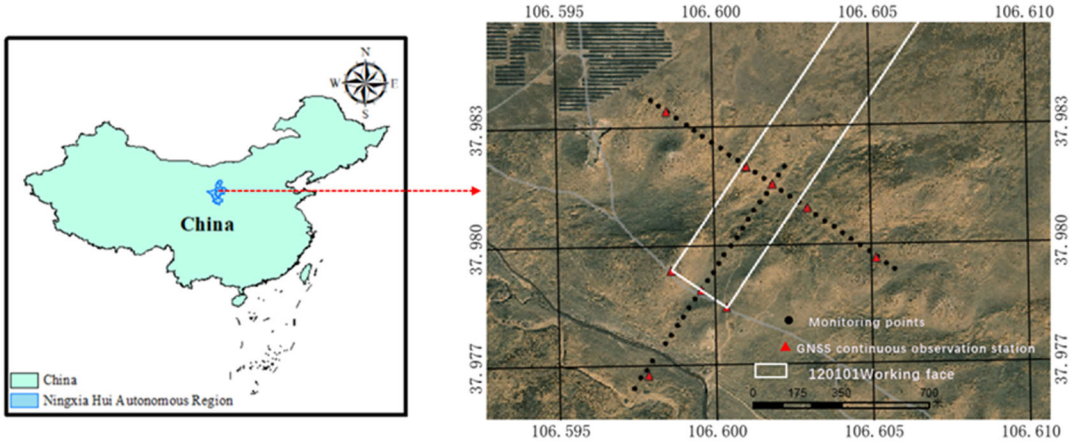

Figure 1. Study area map

2.2. Data Sources

2.2.1. SAR Data

Sentinel-1A is one of the two Earth observation satellites launched under the Copernicus Programme by the European Space Agency (ESA). Equipped with a C-band Synthetic Aperture Radar (SAR), Sentinel-1A can acquire imagery under all weather and lighting conditions and is widely used in topographic mapping and surface deformation monitoring. The data used in this study were downloaded from the official ESA platform. Sentinel-1A has a revisit cycle of 12 days, and precise orbit corrections were applied using the AUX_POEORB orbit files. To ensure temporal consistency with the UAV data, SAR images were selected to match the UAV acquisition dates as closely as possible. Specifically, two Sentinel-1A images acquired on August 10, 2022, and January 9, 2023, were used in this study.

2.2.2. UAV Data

The UAV data were acquired using a DJI multi-rotor drone equipped with a RuiPu RIY-02 camera. The experiment adopted a control-free UAV photogrammetry technique, supported by Real-Time Kinematic (RTK) and Post-Processed Kinematic (PPK) GNSS differential processing to enhance the accuracy of aerial triangulation, thus eliminating the need for ground control points (GCPs). UAV surveys were conducted twice, on August 14, 2022, and December 31, 2022, corresponding to the acquisition dates of the SAR images.Prior to each flight, the UAV flight paths were planned using DJI Pilot software based on the local terrain, elevation differences, and surrounding environment. Flight parameters such as forward and side overlap ratios were set appropriately. During flight, the camera was slightly tilted to improve vertical accuracy. A flight speed of 8 m/s was used considering the study area's conditions. To ensure sufficient detail and spatial resolution, the point cloud density was designed to reach 100 points per square meter.

3. Research Methods

3.1. DInSAR Data Processing

In this study, the processing of SAR data was performed using SARscape (version ENVI 5.6), a module developed by the Swiss company SARMap based on the ENVI remote sensing platform. Two Sentinel-1A images acquired on August 10, 2022, and January 9, 2023, were processed in combination with external DEM data. The differential interferometric SAR (DInSAR) technique was adopted, with the main processing steps including image co-registration, interferogram generation, adaptive filtering for coherence optimization, phase unwrapping, geocoding, and deformation analysis through phase-to-displacement conversion.During the processing, one-dimensional deformation in the radar line-of-sight (LOS) direction was first obtained using the DInSAR technique. The vertical displacement component

was then derived through coordinate transformation, resulting in the generation of subsidence data, as illustrated in Figure 2. DInSAR-derived displacement values at selected monitoring points were extracted and compared with leveling measurements for validation purposes. The comparison results are presented in Figure 3.

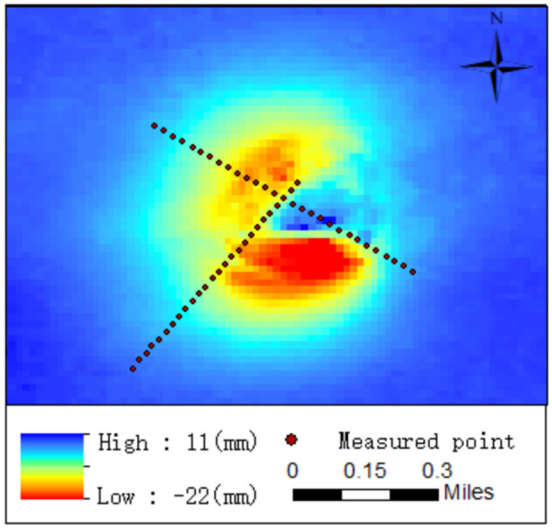

Figure 2. DInSAR processing result

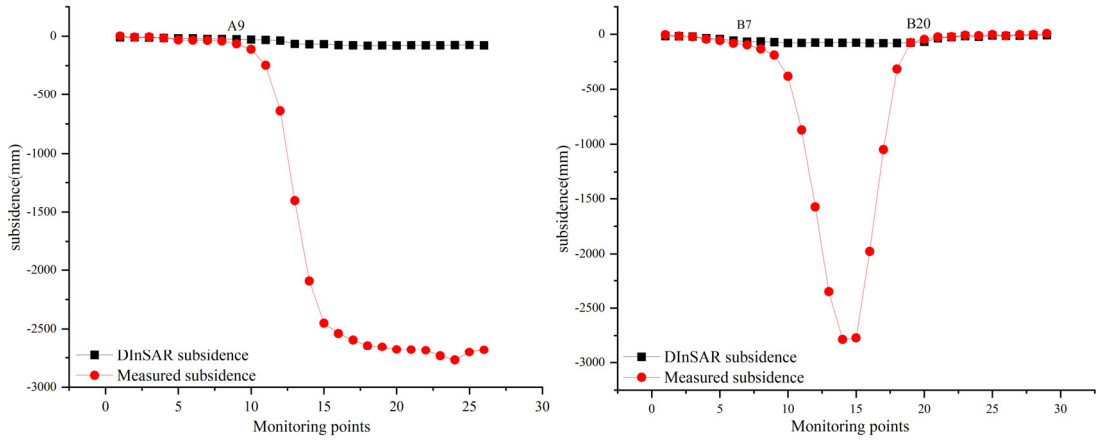

(a) (b)

Figure 3. Comparison of DInSAR Data and Leveling Data along the Strike and the Dip Line

As shown in Figure 3, along the strike observation line, the DInSAR results are generally consistent with the leveling data before the ninth monitoring point (A9). Similarly, along the dip observation line, good agreement is observed before the seventh monitoring point (B7) and after the twenty-third point (B23). However, at other monitoring locations, significant discrepancies arise due to decorrelation effects caused by large-magnitude surface subsidence. Overall, DInSAR can accurately reflect the location, extent, and spatial variation trend of subsidence, aligning well with actual mining activities. Nevertheless, in the central subsidence area, where deformation gradients are high, monitoring accuracy deteriorates significantly. This results in an underestimation of the subsidence magnitude, making it difficult to fully characterize the deformation pattern of the subsidence basin.

3.2. PIM Extracting Deformation in Mining Areas

The Probability Integral Method (PIM), based on the theory of random media, is also known as the random medium model. In the 1950s, the Polish scholar Lityński introduced this concept into the study of rock layer movement. Lityński, based on granular medium theory, investigated the deformation of rock layers and the ground surface caused by mining activities. He postulated that the deformation patterns are similar to the characteristics of random media. The model assumes that the medium is composed of independently moving particles, and the overall deformation is a random process.

Based on this assumption, the method treats the movement of mining rock layers as a random phenomenon that follows a normal distribution and simulates the shape of the surface subsidence basin using a probability density function. According to the PIM theory, for a working face with a strike length of D3 and dip length of D1, the subsidence value at an arbitrary point (x, y) on the surface caused by mining can be expressed as:

$$W(x,y) = \frac{1}{W_0} W^0(x) W^0(y) \tag{1}$$

$$W^0(x) = \frac{W_0}{2}\left\{\frac{2}{\sqrt{\pi}}\int_0^{\sqrt{\pi}\frac{x\tan\beta}{H_0}} e^{-u^2}\,du - \frac{2}{\sqrt{\pi}}\int_0^{\sqrt{\pi}\frac{[x-(D_3-S_3-S_4)]\tan\beta}{H_0}} e^{-u^2}\,du\right\} \tag{2}$$

$$W^0(y) = \frac{W_0}{2}\left\{\frac{2}{\sqrt{\pi}}\int_0^{\sqrt{\pi}\frac{y\tan\beta_1}{H_1}} e^{-u^2}\,du - \frac{2}{\sqrt{\pi}}\int_0^{\sqrt{\pi}\frac{\left[y-(D_1-S_1-S_2)\frac{\sin(\theta+\alpha)}{\sin\theta}\right]\tan\beta_2}{H_3}} e^{-u^2}\,du\right\} \tag{3}$$

$$W_0 = m * q * \cos\alpha \tag{4}$$

In the coordinate system of the working face, W_0 represents the maximum subsidence value, while $W^0(x)$ and $W^0(y)$ represent the subsidence values at the projected points along the strike and dip profiles, respectively. u denotes the mining unit for probability integration, and mmm refers to the coal seam thickness. H_0 is the average mining depth, while H_1 and H_3 represent the mining depths for the downhill and uphill mining areas, respectively. The parameter q is the subsidence coefficient, tanβ is the tangent of the main influencing angle, and $\tan\beta_1$ and $\tan\beta_2$ represent the tangents of the main influencing angles for downhill and uphill mining, respectively. S_3 and S_4 represent the offsets of the inflection points for the left and right boundaries, and S_1 and S_2 represent the inflection point offsets for the downhill and uphill mining areas. θ is the propagation angle of mining influence, and α is the dip angle of the coal seam.

By combining leveling points with the probability integral model and using surface fitting methods, the probability integral parameters for this mining area were inverted as B=[q, tanβ,S_1,S_2,S_3,S_4,θ,b]=[2.1,2.6,91,16,8,24,86∘,0.2]. These parameters were substituted into equations (1), (2), (3), and (4) to calculate the predicted subsidence basin for the 120101 working face of the mining area, as shown in Figure 4. The PIM-derived subsidence values at each monitoring point were extracted and compared with the leveling data for validation, with the results shown in Figure 5.

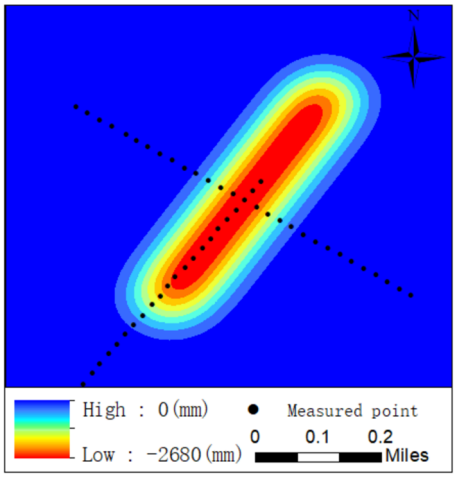

Figure 4. PIM processing result

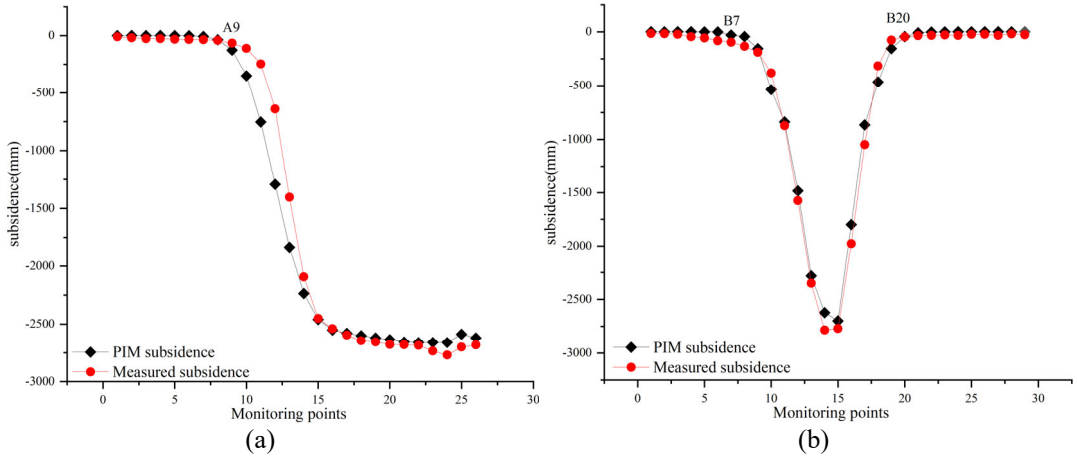

Figure 5. Comparison of DInSAR Data and Leveling Data along the Strike and the Dip Line

As shown in Figure 5, the Probability Integral Method (PIM) detects a distinct funnel-shaped subsidence basin above the 120101 working face, with a maximum subsidence of 2680 mm. The maximum subsidence measured by leveling is 2770 mm, indicating that PIM technology can effectively detect large gradient deformations in the mining area. By comparing the subsidence data obtained from PIM with the leveling data, we find that the error is small near the maximum subsidence value. However, the method shows almost no subsidence occurring around the working face. In summary, PIM technology can monitor the maximum subsidence and reflect the overall subsidence trend, but it is not sensitive to small-scale subsidence.

3.3. UAV Data Processing

UAV photogrammetry combines photogrammetry and remote sensing technology to capture surface images using high-precision cameras, and uses the geometric relationships of multi-angle images along with computer vision algorithms for three-dimensional reconstruction and geographic information extraction. The core principle involves projecting three-dimensional objects onto two-dimensional images using camera imaging models (e.g., pinhole model), and then solving for three-dimensional coordinates using bundle adjustment. During task execution, the UAV collects images based on planned flight paths and overlap in both the forward and side directions, ensuring data redundancy and coverage, which serves as the basis for subsequent image matching and three-dimensional modeling. In the image processing phase, feature point matching technology is used to extract homologous points, and with the help of ground control points (GCP) or GNSS/IMU data, exterior orientation parameters are determined, converting the local coordinate system to the geographic coordinate system. During three-dimensional reconstruction, dense matching algorithms generate a dense point cloud, which is further used to create a Digital Elevation Model (DEM). Subtracting the DEM from December 31, 2022, from the DEM of August 14, 2022, results in the surface subsidence basin between these two time points in the study area (Figure 6). Additionally, UAV monitoring values at each point were extracted and compared with the measured data, as shown in Figure 7.

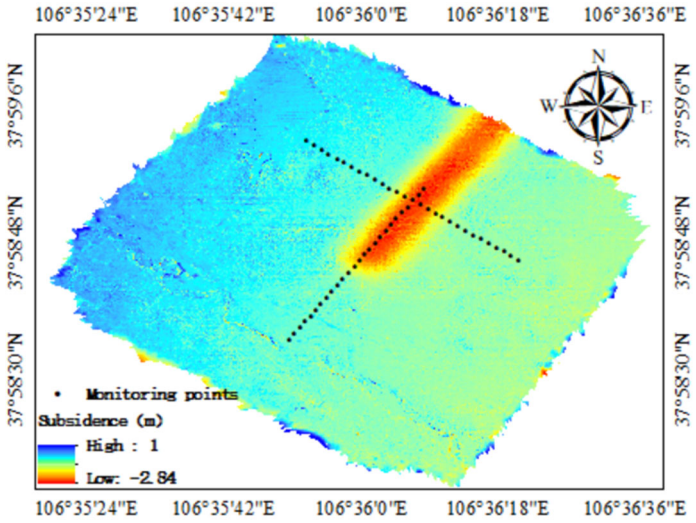

Figure 6. UAV monitoring settlement results

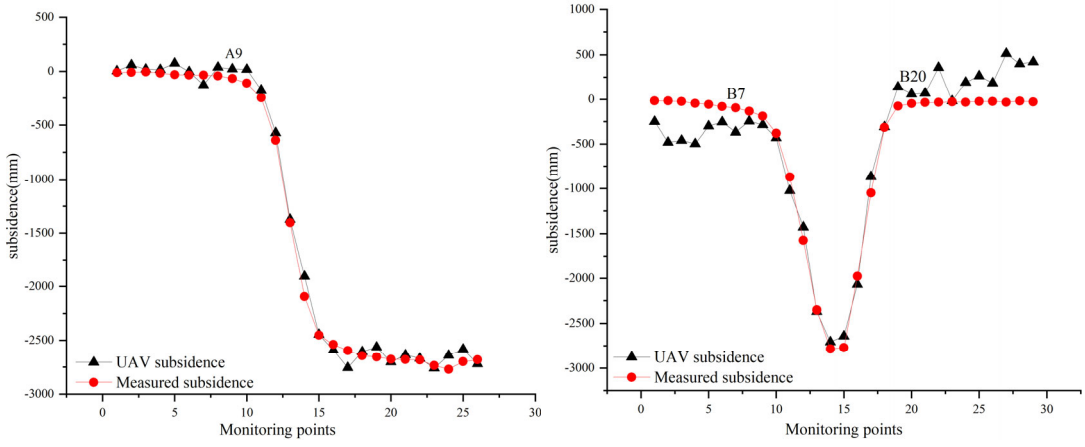

Figure 7. Comparison of the direction and trend line UAV monitoring values and level data

As shown in Figure 8, the comparison between UAV and leveling measurement subsidence data reveals the following

results: along the strike observation line A, the maximum subsidence measured by UAV is 2840 mm, while the leveling measurement is 2770 mm, with a relative error of 2.5%; along the dip observation line B, the UAV measurement is 2727 mm, while the leveling measurement is 2770 mm, with a relative error of 1.5%. The comparison of lines A and B indicates that UAV photogrammetry can accurately capture the maximum subsidence value of the subsidence basin. Furthermore, the monitoring results show that the UAV data has a smaller error in the central region of the subsidence basin, where subsidence is larger, and the subsidence gradient is more pronounced. However, in areas with smaller subsidence or at the edges of the subsidence basin, the error between UAV monitoring data and leveling data is relatively large. In summary, UAV photogrammetry is suitable for monitoring large-gradient and large-magnitude deformations, providing accurate measurements of the maximum subsidence and reflecting the overall subsidence trend. However, there are still limitations in monitoring small deformations at the edges of the subsidence basin, where the monitoring accuracy is relatively lower.

3.4. Fusion of DInSAR, PIM, and UAV Data

From the above data processing results, it is evident that DInSAR can accurately reflect the location, extent, and spatial variation trends of subsidence, consistent with the actual mining conditions of the mining area, with higher accuracy at the edges of the mining area. On the other hand, PIM and UAV-based deformation extraction technologies provide high accuracy at the center of the mining area. Therefore, to comprehensively and accurately monitor and analyze ground subsidence, DInSAR is used to monitor the ground subsidence basin edges with smaller deformations, while PIM and UAV weighted fusion technology is employed to extract the ground subsidence basin center with large-gradient deformations.

3.4.1. DInSAR Monitoring Threshold

Points with a subsidence value of 10 mm are typically used as boundary points for the surface subsidence basin [33]. However, the observation accuracy of differential interferometric synthetic aperture radar (DInSAR) technology can reach the millimeter level. Massonnet and Feigl (1988) introduced the concept of deformation gradient to represent the relative displacement between any two points and defined the maximum deformation gradient that InSAR can monitor.

$$d_{max} = \frac{\lambda}{2\mu} \tag{5}$$

In equation (5), d_{max} represents the maximum deformation gradient that InSAR can theoretically monitor, μ represents the size of a single SAR pixel, and λ denotes the radar wavelength. From equation (5), it can be seen that d_{max} is theoretically closely related to the radar parameters. The longer the radar wavelength and the smaller the pixel size, the larger the deformation gradient that can be monitored. For example, using the C-band Sentinel data with a 1:4 multi-view processing (resolution of 20 meters), the theoretically detectable deformation gradient is 1.4×10−3 m.

Equation (5) is derived under ideal conditions. In practical applications, the maximum deformation gradient monitored by InSAR is inevitably affected by factors such as orbital errors, temporal and spatial decorrelation, and atmospheric delay effects, leading to actual monitored values that are often smaller than the theoretical values. To address this issue, Baran et al. (2005) studied the effect of coherence on InSAR deformation gradient monitoring and proposed a deformation gradient threshold expression based on image coherence.

$$D_{max} = d_{max} + 0.002(\gamma - 1) \tag{6}$$

According to equation (6), the actual maximum detectable deformation gradient D_{max} of InSAR is linearly positively correlated with the image coherence γ. The higher the image coherence, the larger the maximum deformation gradient that InSAR can monitor. For SAR images, there exists a coherence threshold, below which $D_{max}=0$, meaning surface deformation cannot be monitored. For example, for Sentinel images, when the coherence coefficient γ is 0.3, $D_{max}=0$, indicating that surface deformation cannot be monitored when the coherence of Sentinel data is less than 0.3. Therefore, this value is used as the filtering threshold for DInSAR monitoring. The coherence coefficient for each monitoring point was extracted, and for the points beyond A7 along the strike line, the coherence coefficient is less than 0.3, with the value decreasing as it approaches the center. For the dip line, the coherence coefficient between points B5 and B20 is less than 0.3. Thus, DInSAR monitoring is applied to the monitoring points up to A7 and B5, as well as those beyond B20.

3.4.2. Data Fusion

When performing weighted fusion of PIM deformation data and UAV deformation data, known weighting methods for combining different data sources include the average weighting method, the empirical weighting method, and the inverse variance weighting method. The inverse variance weighting method automatically adjusts the weights based on data accuracy. The smaller the variance (i.e., the higher the data quality), the larger the weight, making the fusion result more reliable. Therefore, when performing weighted fusion of PIM data and UAV data, the inverse variance weighting method is often the more advantageous choice. The variance of each indicator is calculated, and the reciprocal of the variance is used as the weight for that indicator, as shown in equation (7).

$$w_j = \frac{\frac{1}{\sigma_i^2}}{\sum_{i=1}^{m} \frac{1}{\sigma_i^2}} \tag{7}$$

In Equation (7), w_j represents the weight of each data source, and σ_i^2 represents the variance between the weighted fusion data source and the actual leveling data.

When performing weighted fusion for DInSAR, PIM, and UAV deformations, DInSAR deformation data is still used for the edge of the mining area, while PIM and UAV data are fused with weights at the center of the mining area. After calculation, the variance between PIM deformation data and leveling data is 183 mm, and the variance between UAV data and leveling data is 111 mm. Using the formula in Equation (7), the weight for PIM data is 0.38, and the weight for UAV data is 0.62. The resulting fused subsidence values are shown in Equation (8).

$$d = \begin{cases} d_{InSAR} & d < 35mm \\ 0.38 * d_{PIM} + 0.62 d_{UAV} & d \geq 35mm \end{cases} \tag{8}$$

After calculation using Equation (8), the fused DInSAR,

PIM, and UAV data were compared with the leveling data, as shown in Figures 8 and 9.

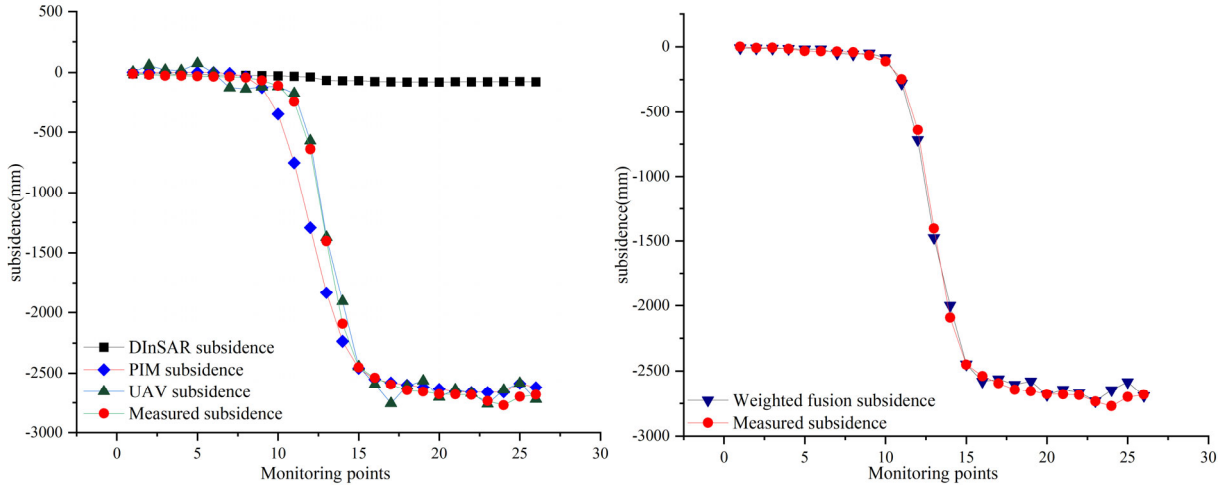

(a) (b)

Figure 8. Comparison of leveling data before and after the fusion of three types of data along the strike line.

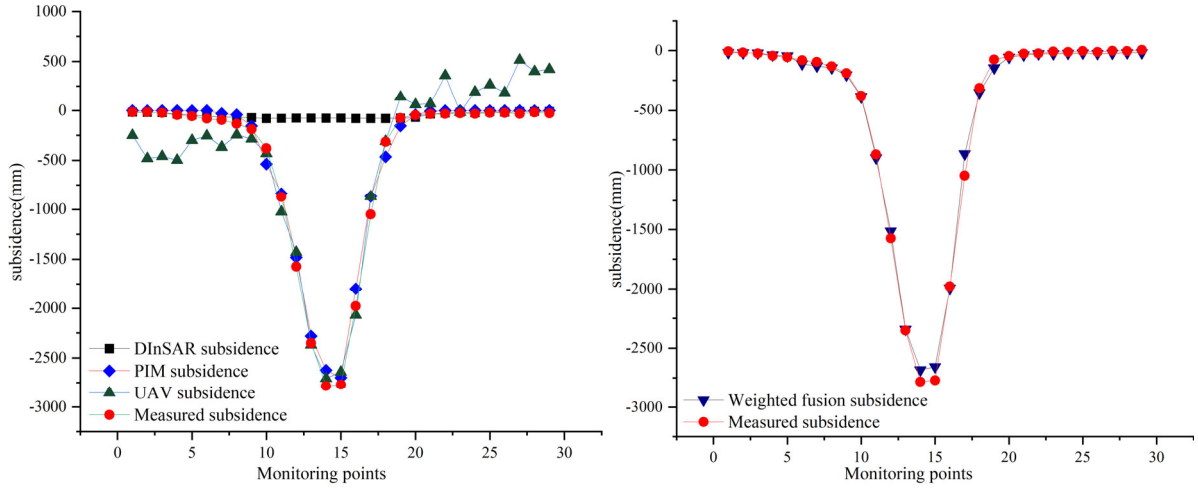

(a) (b)

Figure 9. Comparison of leveling data before and after the fusion of three types of data along the dip line.

Based on Figures 8 and 9, it can be observed that between August 14, 2022, and December 31, 2022, DInSAR, Probability Integral Method (PIM), UAV, and weighted fusion techniques all detected surface subsidence above the 120101 working face. Whether along the strike line or the dip line, the subsidence results obtained through the fusion of the three data types are consistent with the shape and trend of the measured subsidence curve, and they also align with the leveling monitoring results.

4. Accuracy Analysis

To further verify the accuracy of the weighted fusion monitoring results, subsidence data from the 120101 working face of the mining area, including data from DInSAR, PIM, UAV, and the fused data, as well as actual leveling measurements, were collected. The mining area was divided into the edge and the center for analysis. First, based on the measured leveling data and expert judgment, we set a subsidence threshold value of 100 mm to distinguish between the edge and the center of the mining area. The threshold on the strike observation line A is located at point A9, and on the dip observation line B, the thresholds are located at points B7 and B19. Therefore, the edge of the mining area is defined by the regions A1-A9, B1-B7, and B20-B29, while the center of the mining area is defined by A10-A26 and B8-B18.Next, three criteria—Maximum Absolute Error (mm), Mean Absolute Error (MAE (mm)), and Root Mean Square Error (RMSE)—were used to assess the accuracy of the three deformation datasets in the mining area edge and center.

(1) At the Mining Area Edge: The comparison between the DInSAR, PIM, and UAV deformation data and the leveling data is shown in Figure 10. The accuracy of the three deformation datasets in terms of Maximum Absolute Error (mm), Mean Absolute Error (MAE (mm)), and Root Mean Square Error (RMSE) at the mining area edge is presented in Table 1.

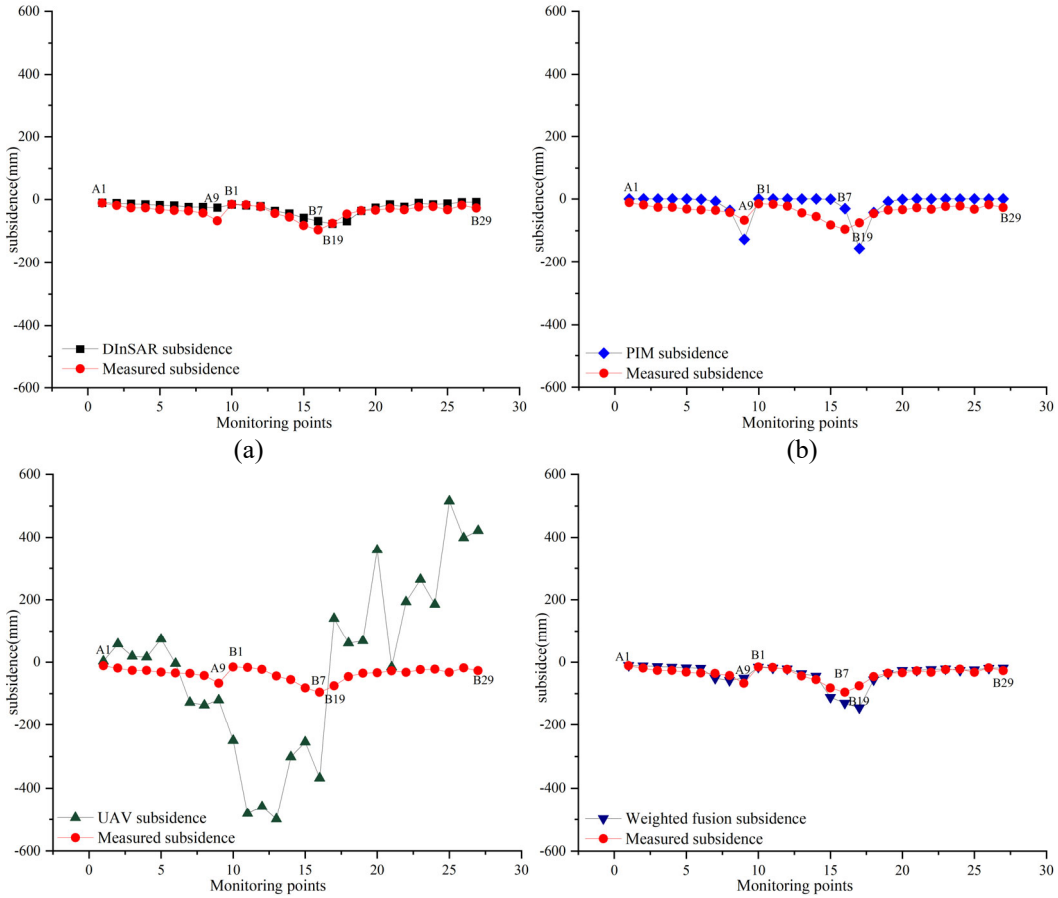

Figure 10. Comparison of the edge of the mining area

From Figure 10, it can be clearly observed that in the edge area of the mining area, the DInSAR deformation data and the data fusion deformation data have a significantly better fit with the leveling data compared to the PIM and UAV data. As for the PIM deformation data, most of the values show 0 mm, indicating that this method is unable to effectively capture the small surface deformations occurring in this region. The UAV deformation data, on the other hand, shows fluctuating patterns with a wider range of variation, and there is a noticeable discrepancy between the UAV data and the leveling data.

Table 1. Comparative analysis of the accuracy of three methods at the edge of the mining area

Methods	Maximum absolute error (mm)	Mean absolute error (mm)	RMSE(mm)
DInSAR	41	12	15
PIM	71	32	37
UAV	547	214	268
Data Fusion	33	9	12

According to the accuracy comparison analysis results of the three methods in Table 1, it is evident that in the edge area of the mining region, the data fusion technique provides the highest accuracy among all the methods after calculating with the three accuracy analysis standards. Next is DInSAR technology, which also shows relatively good accuracy; PIM technology has a moderate level of accuracy; while UAV technology exhibits the lowest accuracy. In the mining area's edge, the deformation values obtained through data fusion show a 20% improvement in accuracy compared to DInSAR technology. This indicates that both techniques can extract subtle deformation features at the mining area's edge, but data fusion is more advantageous than DInSAR, providing higher precision for the edge settlement values. Compared to PIM technology, the accuracy of the deformation values obtained by data fusion improved by 68%, highlighting the limitations of PIM in this region and its difficulty in effectively identifying and quantifying ground deformation like data fusion can. In contrast to UAV technology, the accuracy of the deformation values obtained by data fusion increased by 96%.

(2) In the central area of the mining region, a comparison of DInSAR deformation data, PIM deformation data, and UAV deformation data with leveling data is shown in Figure 11. The accuracy of the three deformation data sets in the central area of the mining region, in terms of maximum absolute error (mm), mean absolute error (MAE (mm)), and root mean square error (RMSE), is presented in Table 2.

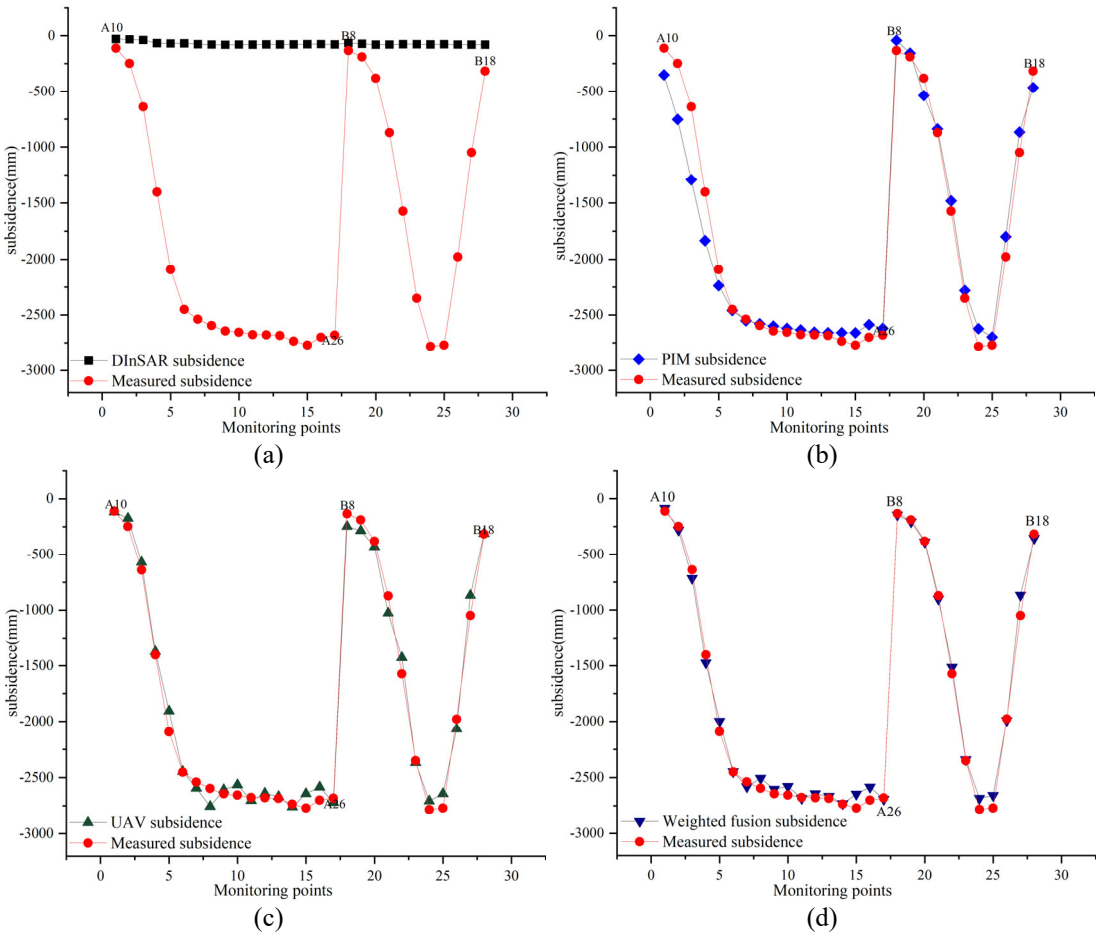

Figure 11. Comparison chart of mining area center

From Figure 11, it is visually apparent that in the central area of the mining region, the deformation data obtained by different technologies show distinct contrast with the leveling data. Specifically, the DInSAR deformation data exhibits a significant discrepancy with the leveling data, indicating that DInSAR technology cannot effectively monitor large-gradient deformations in the mining area. The PIM deformation data shows some differences with the leveling data in the outer region of the mining center but provides a good fit in the center. UAV deformation data, compared to DInSAR and PIM technologies, demonstrates a better fit with the leveling data. However, there is still some discrepancy at the central location. After data fusion, the deformation data successfully combines the strengths of DInSAR, PIM, and UAV technologies, presenting the best fitting results with the leveling data. The data fusion technique, by integrating and processing multiple data sources, effectively compensates for the limitations of individual technologies in the complex environment of the mining area center, offering a more accurate representation of the actual ground deformation in the central mining region.

Table 2. Comparative analysis of the accuracy of the three methods in the mining area center

Methods	Maximum absolute error (mm)	Mean absolute error (mm)	RMSE(mm)
DInSAR	2705	1739	2011
PIM	654	134	203
UAV	186	77	130
Data Fusion	181	51	68

The precision comparison analysis of the four methods calculated from Table 2 shows that, in the mining area center, the data fusion technique yields the highest accuracy for ground subsidence values, followed by UAV technology and PIM technology, with DInSAR technology having the lowest precision. After calculations, it is found that the precision of the mining area deformation extracted using the data fusion technique in the center of the mining area improved by 48%, 67%, and 97% compared to the deformation extraction precision of UAV, PIM, and DInSAR, respectively.

5. Conclusion

This paper addresses the shortcomings of DInSAR, PIM, and UAV technologies in extracting surface deformation in mining areas, and proposes a method for integrating these three technologies to achieve mining area deformation extraction. Using the 120101 working face of the Yangchangwan Coal Mine as the research area, the method was applied to extract the mining area deformation and successfully obtained the subsidence basin in the study period. By comparing and analyzing the DInSAR deformation data,

PIM deformation data, UAV data, and leveling data, the following key conclusions were drawn:

(1) Comparison of DInSAR, PIM, and UAV Extracted Mining Area Deformation:In the mining area edge region, DInSAR technology exhibited higher accuracy, while the accuracy of mining area deformation extracted using UAV technology was lowerIn contrast, in the mining area center, UAV technology provided the highest accuracy for mining area deformation extraction, while DInSAR could not monitor large-gradient deformations in the mining area.

(2) Proposed Data Fusion Method for DInSAR, PIM, and UAV:A data fusion method integrating DInSAR, PIM, and UAV data was proposed and compared with DInSAR, PIM, and UAV data fusion alone.Comparison of the deformation data obtained from the four methods with measured data showed that:In the mining area edge, the fusion of DInSAR, PIM, and UAV data improved the precision by 20%, 68%, and 96%, respectively, compared to DInSAR, PIM, and UAV data alone; In the mining area center, the fusion of DInSAR, PIM, and UAV data improved the precision by 97%, 67%, and 48%, respectively, compared to DInSAR, PIM, and UAV data alone.

References

[1] Fan, H.; Gao, X.; Yang, J.; Deng, K.; Yu, Y. Monitoring Mining Subsidence Using A Combination of Phase-Stacking and Offset-Tracking Methods. Remote Sens.2015,7, 9166-9183.

[2] Sahoo, S.; Khaoash, S. Impact assessment of coal mining on groundwater chemistry and its quality from Brajrajnagar coal mining area using indexing models. J. Geochem. Explor. 2020, 215, 0375-6742.

[3] Bell, F.; Stacey, T.; Genske, D. Mining subsidence and its effect on the environment: some differing examples. Environ. Geol.2000, 40, 135–152.

[4] Yang Z, Li Z, Zhu J, et al. Use of SAR/InSAR in mining deformation monitoring, parameter inversion, and forward predictions: A review. IEEE Geoscience and Remote Sensing Magazine, 2020, 8(1): 71-90.

[5] Chen Y, Tong Y, Tan K. Coal mining deformation monitoring using SBAS-InSAR and offset tracking: A case study of Yu County, China. IEEE Journal of Selected Topics in Applied Earth Observations and Remote Sensing, 2020, 13: 6077-6087.

[6] Yan, W.; Chen, Z.; Chen, J.; Zhao, C. Spatiotemporal Patterns of Vegetation Evolution in a Deep Coal Mining Subsidence Area: A Remote Sensing Study of Liangbei, China. Remote Sens. 2024, 16, 3204.

[7] Chao L, Jian W, Zeng-ke L I, et al. A new method for mining deformation monitoring with GPS-RTK. Transactions of Nonferrous Metals Society of China, 2011, 21: s659-s664.

[8] Jing-Xiang G, Hong H. Advanced GNSS technology of mining deformation monitoring. Procedia Earth and Planetary Science, 2009, 1(1): 1081-1088.

[9] Hao W, Chuang H, Jianhua Z, et al. Deformation Monitoring System for High Slope in Open Pit Mine with the Integration of GNSS and GIS. Geomatics & Information Science of Wuhan University, 2015, 40(5)

[10] WANG G, XU Y, CHENG X, et al. A study of GPS ground deformation monitoring of Jinfeng coal mine in Ningdong coal base. Geological Bulletin of China, 2018, 37(12): 2199-2207.

[11] Yang Z, Li Z, Zhu J, et al. Use of SAR/InSAR in mining deformation monitoring, parameter inversion, and forward predictions: A review. IEEE Geoscience and Remote Sensing Magazine, 2020, 8(1): 71-90.

[12] Chen Y, Tong Y, Tan K. Coal mining deformation monitoring using SBAS-InSAR and offset tracking: A case study of Yu County, China. IEEE Journal of Selected Topics in Applied Earth Observations and Remote Sensing, 2020, 13: 6077-6087.

[13] Li Y, Yang K, Zhang J, et al. Research on time series InSAR monitoring method for multiple types of surface deformation in mining area. Natural Hazards, 2022, 114(3): 2479-2508.

[14] Wang F, Tao Q, Liu G, et al. Monitoring of surface deformation in mining area integrating SBAS InSAR and Logistic Function. Environmental Monitoring and Assessment, 2023, 195(12): 1493.

[15] Chen B, Deng K, Fan H, et al. Large-scale deformation monitoring in mining area by D-InSAR and 3D laser scanning technology integration. International Journal of Mining Science and Technology, 2013, 23(4): 555-561.

[16] Parizzi A, Brcic R, De Zan F. InSAR performance for large-scale deformation measurement. IEEE Transactions on Geoscience and Remote Sensing, 2020, 59(10): 8510-8520.

[17] Wang L, Deng K, Fan H, et al. Monitoring of large-scale deformation in mining areas using sub-band InSAR and the probability integral fusion method. International Journal of Remote Sensing, 2019, 40(7): 2602-2622.

[18] Hu J, Li Z W, Ding X L, et al. Resolving three-dimensional surface displacements from InSAR measurements: A review. Earth-Science Reviews, 2014, 133: 1-17.

[19] Wang Z, Yu S, Tao Q, et al. A method of monitoring three-dimensional ground displacement in mining areas by integrating multiple InSAR methods. International Journal of Remote Sensing, 2018, 39(4): 1199-1219.

[20] Fan H, Wen B, Liu J, et al. An improved method of three-dimensional displacement field generation in mining areas with a single InSAR pair. European Journal of Remote Sensing, 2019, 52(1): 493-503.

[21] Xia Y, Wang Y. InSAR-and PIM-based inclined goaf determination for illegal mining detection. Remote Sensing, 2020, 12(23): 3884.

[22] WANG Z H, LIU J B, YAN Y G, et al. SGI-based method combined with PIM for subsidence calculation of the total basin in mining area. Progress in Geophysics, 2023, 38(6): 2440-2450.

[23] Wang L, Jiang K, Wei T, et al. Estimation of parameters of probability integral method model based on improved fireworks algorithm. Survey Review, 2021, 53(379): 366-382.

[24] Lou J. A parameter inversion method for the probability integral method based on robust ridge estimation. Frontiers in Earth Science, 2024, 11: 1330163.

[25] Tao T, Zhao G, Yu Y, et al. A fully adaptive method for structural stochastic response analysis based on direct probability integral method. Computer Methods in Applied Mechanics and Engineering, 2022, 396: 115066.

[26] Ćwiąkała P, Gruszczyński W, Stoch T, et al. UAV applications for determination of land deformations caused by underground mining. Remote Sensing, 2020, 12(11): 1733.

[27] Zhan X, Zhang X, Wang X, et al. Comparative analysis of surface deformation monitoring in a mining area based on UAV-lidar and UAV photogrammetry. The Photogrammetric Record, 2024, 39(186): 373-391.

[28] Ren H, Zhao Y, Xiao W, et al. A review of UAV monitoring in mining areas: Current status and future perspectives. International journal of coal science & technology, 2019, 6: 320-333.

[29] Ignjatović Stupar D, Rošer J, Vulić M. Investigation of unmanned aerial vehicles-based photogrammetry for large mine subsidence monitoring. Minerals, 2020, 10(2): 196.

[30] Dorokhov D V, Nizametdinov F K, Ozhigin S G, et al. A Technique for surveying of ground surface deformations in mine field. Journal of Mining Science, 2018, 54: 874-882.

[31] Chand K, Mankar A K, Koner R, et al. Dump slope change detection and displacement monitoring using UAV close-range photogrammetry. Sādhanā, 2024, 49(4): 277.

[32] Zhu M, Yu X, Tan H, et al. Integrated high-precision monitoring method for surface subsidence in mining areas using D-InSAR, SBAS, and UAV technologies. Scientific Reports, 2024, 14(1): 12445.

[33] Tan H, Yu X, Zhu M, et al. Deformation Monitoring and Spatiotemporal Evolution of Mining Area with Unmanned Aerial Vehicle and D-InSAR Technology. Mobile Information Systems, 2022, 2022(1): 8075611.

[34] Chen X, Chen J, Wang G, et al. Mining Subsidence Based on Integrated SBAS-InSAR and Unmanned Aerial Vehicles Technology. Journal of Ocean University of China, 2024: 1-17.

[35] ZHOU D, AN S, WU K, et al. Key technology and application of InSAR/UAV fusion monitoring for coal mining damages. Coal Science and Technology, 2022, 50(10): 121-134.

[36] Dawei Z, Lizhuang Q, Demin Z, et al. Unmanned aerial vehicle (UAV) photogrammetry technology for dynamic mining subsidence monitoring and parameter inversion: A case study in China. IEEE Access, 2020, 8: 16372-16386.

[37] Zhou, D., Wang, L., An, S.et al. Integration of unmanned aerial vehicle (UAV)-based photogrammetry and InSAR for mining subsidence and parameters inversion: a case study of the Wangjiata Mine, China. Bull Eng Geol Environ, 2022,81, 343.

[38] Yang B, Du W, Zou Y, et al. Reconstruction of Coal Mining Subsidence Field by Fusion of SAR and UAV LiDAR Deformation Data. Remote Sensing, 2024, 16(18): 3383.

[39] Chi S, Yu X, Wang L. Method of Predicting Dynamic Deformation of Mining Areas Based on Synthetic Aperture Radar Interferometry (InSAR) Time Series Boltzmann Function. Applied Sciences, 2024, 14(17): 7917.